Journal of
Composites Science

MDPI

Article

Crack Assessment Using Acoustic Emission in Cement-Free High-Performance Concrete Under Mechanical Stress

Muhammad Ali Rostampour *, Davood Mostofinejad, Hadi Bahmani and Hasan Mostafaei *

Department of Civil Engineering, Isfahan University of Technology (IUT), Isfahan 84156-83111, Iran; dmostofi@iut.ac.ir (D.M.); h.bahmani@cv.iut.ac.ir (H.B.)
* Correspondence: ma.rostampour@cv.iut.ac.ir (M.A.R.); h.mostafaei@cv.iut.ac.ir (H.M.)

Abstract

This study investigates the cracking behavior of high-performance calcium oxide-activated concrete incorporating basalt and synthetic macro fibers under compressive and flexural loading. Acoustic emission (AE) monitoring was employed to capture real-time crack initiation and propagation, offering insights into damage evolution mechanisms. A comprehensive series of uniaxial compression and four-point bending tests were conducted on fiber-reinforced and plain specimens. AE parameters, including count, duration, risetime, amplitude, and signal energy, were analyzed to quantify crack intensity and classify fracture modes. The results showed that tensile cracking dominated even under compressive loading due to lateral stresses, while fiber inclusion significantly enhanced toughness by promoting distributed microcracking and reducing abrupt energy release. Basalt fibers were particularly effective under flexural loading, increasing the post-peak load-bearing capacity, whereas synthetic macro fibers excelled in minimizing tensile crack occurrence under compression.

Keywords: sustainable high-performance concrete; acoustic emission; crack propagation monitoring; slag; calcium oxide; basalt fiber; synthetic macro fiber

check for updates

Academic Editor: Peng Zhang

Received: 14 June 2025
Revised: 12 July 2025
Accepted: 18 July 2025
Published: 19 July 2025

Citation: Rostampour, M.A.; Mostofinejad, D.; Bahmani, H.; Mostafaei, H. Crack Assessment Using Acoustic Emission in Cement-Free High-Performance Concrete Under Mechanical Stress. *J. Compos. Sci.* **2025**, *9*, 380. https://doi.org/10.3390/jcs9070380

Copyright: © 2025 by the authors. Licensee MDPI, Basel, Switzerland. This article is an open access article distributed under the terms and conditions of the Creative Commons Attribution (CC BY) license (https://creativecommons.org/licenses/by/4.0/).

1. Introduction

Concrete cracking represents one of the most critical indicators of damage in concrete structures, significantly influencing their mechanical behavior and durability [1]. During compressive and flexural testing, cracks typically progress from the formation of microcracks to the propagation of macrocracks, ultimately leading to specimen failure. Analyzing crack development provides a fundamental understanding of failure mechanisms, stress–strain behavior, and material deficiencies. The evaluation of cracking behavior in these tests serves as a key indicator of mechanical performance, revealing mix design flaws [2]. For instance, the gradual or sudden release of energy during loading, along with corresponding crack propagation patterns, reflects the bonding quality between the aggregates and the cement matrix. In compressive tests, crack formation and propagation in high-performance concrete (HPC) directly manifest the cement matrix strength, paste-aggregate interfacial transition zone (ITZ) bonding, and internal stress distribution [3–5]. Flexural tests demonstrate direct correlations between crack characteristics (including density and width) and critical parameters, such as flexural strength, fracture energy, and post-cracking performance. This assessment enables the identification of mix design weaknesses while providing essential data for material optimization.

Among the various crack detection methodologies, imaging techniques offer surface-level crack monitoring capabilities; however, their effectiveness is often limited to accessible specimen surfaces, as most conventional cameras fail to detect fine microcracks unless expensive high-resolution systems are employed. In contrast, acoustic emission (AE) monitoring emerges as a powerful alternative for comprehensively assessing crack development, proving particularly valuable for evaluating concrete strength and predicting service life. This technique, implemented through piezoelectric sensors mounted on loaded specimens, detects ultrasonic signals emitted during microcrack formation, often identifying damage initiation during the early loading stages before it becomes visually apparent. Through sophisticated signal analysis in both compressive and flexural testing regimes, AE enables the precise characterization of failure mechanisms, critical stress thresholds, and the assessment of concrete quality with remarkable accuracy, providing real-time insights into the degradation processes of structural integrity.

A distinct category exhibiting fundamentally different crack propagation behavior compared to conventional concrete is HPC. Characterized by its low water-to-cement ratio and denser microstructure, HPC demonstrates exceptional mechanical properties, typically achieving compressive strengths exceeding 50–55 MPa and flexural/tensile strengths above 6.5–8 MPa [6,7]. These enhanced characteristics stem primarily from the material's optimized microstructural density. However, the increased brittleness resulting from reduced permeability and the heightened cement matrix density leads to more abrupt cracking patterns in HPC, typically manifesting as a distributed microcrack network rather than localized macro-fractures. Consequently, researchers have endeavored to reinforce the structural elements made of such concrete (particularly ultra HPC, known as UHPC) using various fiber types, either individually or in hybrid configurations, with special emphasis on plate or panel applications [8,9]. AE-based damage quantification parameters—including event counts, released energy, and signal frequency characteristics—prove particularly valuable for evaluating both crack propagation and damage severity in HPC systems, providing critical insights into their unique failure mechanisms [10,11].

This study presents the first investigation into crack development in CaO-activated slag-based concrete using acoustic emission monitoring. Uniaxial compressive and four-point bending tests were conducted on cylindrical and prismatic specimens of calcium oxide-activated slag-based HPC. To control crack distribution and enhance toughness, three different percentages of macro-synthetic fibers and natural basalt fibers were incorporated in the base mix. Simultaneous AE monitoring using two sensors (for compressive tests) and four sensors (for flexural tests) tracked crack development during mechanical testing. The results were analyzed through the time-dependent curves of compressive stress and maximum tensile stress, correlated with AE energy and count parameters. The AE technique effectively identified elastic-to-inelastic transitions without prior knowledge of stress–strain behavior. Fiber reinforcement significantly improved toughness, as evidenced by AE parameter trends that showed a more gradual energy release and distributed cracking. Furthermore, AE analysis enabled crack-type discrimination during both compressive and tough testing phases.

1.1. Sustainable High-Performance Concrete

The conventional HPC mix design typically contains high cement content as its primary component [12,13]. Although increasing the cement content in concrete enhances compressive strength and reduces the dimensions of structural elements and concrete consumption in buildings, Mostafaei et al. [14] demonstrated that structures with higher compressive strength may exhibit greater overall environmental impacts compared to those with lower compressive strength. Therefore, due to the environmental concerns associated

with cement production [15], researchers are actively pursuing strategies to reduce the use of cement in HPC formulations [16]. An alternative approach involves geopolymer concrete technology, which replaces Portland cement with alternative binders consisting of base materials and activators. Ambily et al. [17] developed ultra-high-performance geopolymer concrete incorporating slag, fly ash, and silica fume, achieving remarkable 28-day compressive and flexural strengths of 175 MPa and 13.5 MPa under standard curing conditions. Meanwhile, Wetzel and Middendorf [18] investigated silica fume as partial slag replacement in ultra-high-performance geopolymer concrete with a constant metakaolin content, obtaining a maximum compressive strength of 178.6 MPa with 12.5% silica fume substitution. They observed a reduction in strength at a 15% silica fume content and noted that curing at 60 °C enhanced the development of strength. Most geopolymer-based HPC studies employ potent alkaline activators, such as sodium hydroxide, which present practical challenges, including rapid setting, economic inefficiency, energy-intensive production, and high pH handling risks [19,20]. As a solution, this study utilizes calcium oxide as a low-risk and cost-effective alkaline earth activator for slag, previously validated by the authors in ref. [21], to enable the mass production of environmentally friendly HPC. Their findings demonstrate how this mix design resulted in not only a 4.55% reduction in compressive strength and an 11.6% decrease in flexural strength compared to conventional cement-based HPC, but it also achieved a remarkable 61% reduction in carbon footprint, offering significant environmental benefits. Furthermore, the incorporation of fibers into the slag-based concrete was shown to compensate for its flexural strength limitations effectively. Notwithstanding these demonstrated advantages, the practical and widespread use of this concrete in construction still requires further research. In addition to addressing mechanical performance under various loading conditions—such as dynamic loads—greater attention must be given to the durability of this concrete under different environmental conditions. Challenges also remain regarding large-scale production, curing under site conditions, and the potential influence of real-size elements compared to laboratory-scale specimens. Moreover, the development and optimization of effective admixtures for such concrete types warrant more in-depth investigation. This research incorporates acoustic emission testing to analyze crack propagation during the mechanical testing of this novel sustainable concrete.

1.2. Acoustic Emission

Acoustic emission refers to the phenomenon where transient elastic waves propagate through a material due to rapid energy release from localized sources [22,23]. These waves can be detected by piezoelectric sensors, allowing for the identification of defect type, location, and severity through signal analysis. In homogeneous and isotropic media, AE waves propagate spherically from the source with energy dissipation proportional to distance. However, in concrete structures, wave attenuation occurs due to material porosity, heterogeneity, and aggregate presence [24,25], typically resulting in the lower frequency of emissions. Real-time AE signal processing enables the instantaneous monitoring of concrete behavior, facilitating the early detection of hidden damage before it leads to critical failure. Furthermore, AE serves as a powerful tool for evaluating concrete's mechanical performance and durability characteristics [26–29], offering valuable insights for optimal mix design formulation.

Acoustic emission testing requires specialized hardware and software systems, with equipment costs varying significantly depending on application requirements, specimen characteristics, environmental conditions, and budget constraints. When an AE source activates, each sensor independently detects the emission events, converting them into electrical voltage signals. The complete signal pathway from source to digitized waveform

involves the following multiple stages: (1) AE generation at the source; (2) propagation through the material; (3) transmission across material boundaries; (4) the coupling medium; (5) piezoelectric sensor conversion; (6) signal transmission via coaxial cables; (7) pre-amplification; and finally (8) analog-to-digital conversion in the data acquisition system (DAQ). Figure 1 schematically illustrates the signal chain, along with the corresponding equipment components, for a two-channel AE monitoring setup.

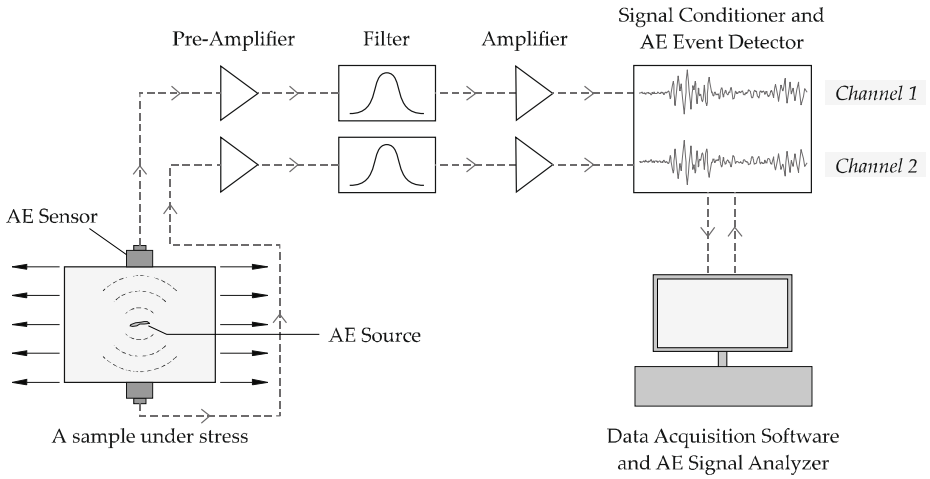

Figure 1. Different components of acoustic emission testing and required equipment.

The data acquisition system requires proper parameter configuration to capture targeted AE events effectively. Three critical timing parameters—peak definition time (PDT), hit definition time (HDT), and hit lockout time (HLT)—must be carefully set by the operator before testing, along with appropriate threshold values, to ensure accurate AE signal recording [30–32]. These system parameters govern the DAQ's ability to distinguish between valid AE hits and background noise during the monitoring process.

2. Materials and Methods

2.1. Experimental Materials

In this study, slag and its activator, calcium oxide (CaO), were used as the primary precursors for synthesizing a geopolymer binder. The slag used had a specific surface area (Blaine fineness) of 480 m^2/kg, conforming to the specifications outlined in Table 1. To activate the slag, calcium oxide powder with a comparable Blaine fineness was utilized. The physicochemical properties of both materials are detailed in the same table.

Table 1. The chemical compositions of the slag and calcium oxide, as provided by the manufacturer (data are given as the weight percentage).

Chemical Name	Chemical Formula	Slag (%)	Calcium Oxide (%)
Aluminum oxide	Al_2O_3	15.5	0.13
Silicon dioxide	SiO_2	36	0.9
Iron (III) oxide	Fe_2O_3	1.15	0.08
Calcium oxide	CaO	38	94
Sulfur trioxide	SO_3	0.5	0.06
Magnesium oxide	MgO	8.7	0.5
Potassium oxide	K_2O	0.5	-
Sodium oxide	Na_2O	0.5	-
Chlorine	Cl	0.02	-
Disulfur	S_2	1.3	-
Manganese (III) oxide	Mn_2O_3	1.5	-
Titanium dioxide	TiO_2	1.4	-
Calcium carbonate	$CaCO_3$	-	2.2
Loss on ignition	LOI	0.25	2.2

In this study, considering the crucial role of aggregate gradation in high-strength concrete, silica sand with particle sizes ranging from 50 to 150 μm was selected. A lignosulfonate-based polycarboxylate superplasticizer, compliant with ASTM C494/C494M-24 [33] type F requirements, was employed to ensure compatibility with geopolymer materials. To enhance the ductility and toughness of flexural specimens and control their cracking behavior, two distinct types of fibers were incorporated. The first comprised natural basalt fibers (BFs), measuring 6 mm in length and 0.56 mm in diameter, with a specific weight of 2800 kg/m^3 and a tensile strength of 1000 MPa. The second utilized synthetic macro fibers (SMFs) with a specific weight of 910 kg/m^3, characterized by a length of 50 mm, a diameter of 0.4 mm, and a tensile strength of 600 MPa. Considering that fiber specifications may vary depending on the manufacturer, the authors attempted to use fibers with properties closely matching those of optimized basalt and synthetic macro fibers used by other researchers in their own specimens [34–38].

2.2. Mix Design and Specimen Preparation

The test specimens in this study consisted of four mix designs, as detailed in Table 2. The first mix design was fiber-free, while the subsequent three mixes incorporated basalt fibers at volumetric fractions of 1.5%, 2%, and 2.5%, respectively. Considering both the concrete mixer's performance and required slump characteristics, these percentages represent the highest optimal fiber contents previously employed by the authors for fiber-reinforced concrete production [21]. The last three mixes used synthetic macro fibers at the exact same percentages as the basalt fibers. All mix designs maintained an identical powder content. However, in the 2.5% fiber mix, an additional superplasticizer was introduced to achieve adequate workability.

Table 2. Concrete mixture proportions (kg/m^3).

Designation	Slag	Calcium Oxide	Silica Sand	Water [1]	Superplasticizer	Fiber
HPC	990	110	1100	220	16	-
HPC-BF1.5	990	110	1100	220	28	42
HPC-BF2.0	990	110	1100	220	28	56
HPC-BF2.5	990	110	1100	220	30	70
HPC-SMF1.5	990	110	1100	220	28	13.65
HPC-SMF2.0	990	110	1100	220	28	18.2
HPC-SMF2.5	990	110	1100	220	30	22.75

[1] A water-to-cement ratio of 20% was maintained for all the mixtures.

The specimens were prepared in the laboratory using a high-speed mixer. Initially, the powdered materials, including slag and silica sand, were mixed for 5 min. Subsequently, the superplasticizer was blended with a portion of the water and added to the mixture. Mixing continued for an additional 3 min to ensure the uniform dispersion of the powder components and prevent any potential segregation or clumping. In a separate container, the remaining water was combined with calcium chloride and introduced into the mixer. The mixture was then mixed for a further 2 min. For compositions containing synthetic macro fibers, after thoroughly mixing the materials, the mixer was set to high speed, and the fibers were gradually and carefully added. The mixer operated at high speed for an additional 5 min to ensure the homogeneous distribution of the fiber.

Immediately after concrete preparation, the slump test was conducted in accordance with ASTM C1437 [39]. The superplasticizer dosage was carefully selected to maintain a target slump of approximately 190 mm while keeping the water-to-cement ratio constant. The cast specimens were demolded after 2 days and subsequently cured in a water tank at room temperature (maintained between 19 °C and 25 °C) for 28 days to ensure proper hydration and strength development.

2.3. Compression Test

Cylindrical specimens (200 × 100 mm^2) were tested for uniaxial compressive strength at 56 days in accordance with ASTM C39/C39M-24 [40], utilizing a 100 t hydraulic compression jack. The displacement-controlled loading was applied at a constant rate of 1 mm/min.

2.4. Flexural Toughness Test

The four-point flexural strength test was conducted on concrete prisms (330 × 70 × 30 mm^3) in accordance with ASTM C78/C78M-22 [41], employing displacement-controlled loading at a rate of 0.45 mm/min. The load from the kN capacity hydraulic jack was applied to the specimens in a four-point bending configuration, using three equal spans of 100 mm each.

2.5. Acoustic Emission Test

Figure 2 illustrates the experimental setup for concrete compressive strength testing, which incorporates both imaging equipment and AE monitoring systems. The SAEU3H * (manufactured by Qingcheng AE Institute Guangzhou, China) four-channel AE system was equipped with G150/1 resonant sensors (frequency range: 60–400 kHz; resonant frequency: 150 kHz) with a minimum sensitivity of 75 dB. The system's frequency response conforms to ASTM E750 [42], exhibiting less than ±3 dB variation across the operational range. Frequency-dependent nonlinearities were compensated through periodic calibrations using reference signals generated by a function generator. Two AE sensors were mounted on cylindrical specimens, and four were mounted on prismatic specimens, though the results from only one channel are presented. Additional channels were analyzed to verify the repeatability of the experimental outcomes. Before sensor installation, the specimen surfaces were sanded, and acoustic grease was applied as a coupling agent to ensure the optimal transmission of mechanical waves. Following reference [43], the timing parameters were set to 50 µs (PDT), 200 µs (HDT), and 300 µs (HLT), with a 39 dB threshold established after evaluating the laboratory conditions and mechanical equipment vibrations. A pre-amplifier gain of 40 dB was selected for an optimal signal-to-noise ratio. System verification was performed through standardized pencil-lead break (PLB) tests before all compressive and flexural experiments, with calibration conducted via simulated AE event localization and data repeatability assessment in accordance with ISO 16,836 [44] and ASTM E976–15 [45] standards for concrete testing.

Figure 2. Test setup, including an acoustic emission system, for a compressive strength test.

The acoustic emission response was captured as time-domain electrical signals by the sensors and transmitted to the AE DAQ system. Various analytical approaches exist for processing these signals, with the majority of research focusing on parametric analysis. Standards and researchers have established multiple time-domain AE parameters, which were categorized in this study into two distinct groups for evaluation: crack intensity indices and crack-type classification indices [46–49], providing unique insights into the material's fracture behavior.

2.5.1. Crack Intensity Indices

Among the acoustic emission parameters, hit and count serve as fundamental indices for the preliminary evaluation of AE test results. A sudden increase in the cumulative curves of these parameters typically indicates the specimen's failure threshold.

- Each threshold-crossing AE signal that satisfies the timing parameters (PDT, HLT, and HDT) constitutes a hit, with its period referred to as the duration [50]. The history of hits itself serves as an analytical approach for damage detection and the assessment of failure severity.
- Count represents the number of threshold crossings made by an AE signal. This parameter depends not only on the noise-filtering threshold but also on the amplifier gain coefficient and coupling efficiency.
- Absolute AE energy provides a measurable index for each emission event, calculated as the area between the signal envelope and threshold line during the hit duration. This energy measurement reflects the actual energy released during crack propagation in the specimen. Studies demonstrate a direct correlation between AE signal energy and both the compressive and flexural strength of concrete [47,51].

2.5.2. Crack-Type Classification Index

The frequency-domain analysis of AE signals enables discrimination between tensile and shear cracks in concrete. The Japanese JCMS-III B5706 [52] standard classifies cracks into tensile and shear types based on two key parameters: the rise angle (RA) and average frequency (AF). These parameters are calculated as follows: RA is defined as the ratio of the risetime to peak amplitude (Equation (1)), while AF represents the count-to-duration ratio (Equation (2)). Here, amplitude refers to the maximum signal voltage during the duration of a hit, and risetime denotes the time from the AE hit onset to peak amplitude attainment.

$$\mathrm{RA} = \frac{\text{Risetime}}{\text{Amplitude}} \tag{1}$$

$$\mathrm{AF} = \frac{\text{Counts}}{\text{Duration}} \tag{2}$$

The classification of crack types was achieved by plotting the RA and AF values for each AE hit in a two-dimensional coordinate system (similar to Figure 3) and analyzing the distribution patterns of these values. This classification suggests that cracks exhibiting high AF and low RA values are tensile in nature, while the inverse relationship applies to shear cracks. By examining the scatter of data points within the two defined regions of this plot, the prevailing failure mode can be reliably determined at any stage of the monitoring process. The ISO 16838:2019 [53] standard has also proposed the classification of crack types based on this same principle, which was utilized in the present research. According to this standard, the slope of the crack classification line (dividing line) is taken as 0.1, with the AF and RA axes expressed in kHz and ms/V, respectively.

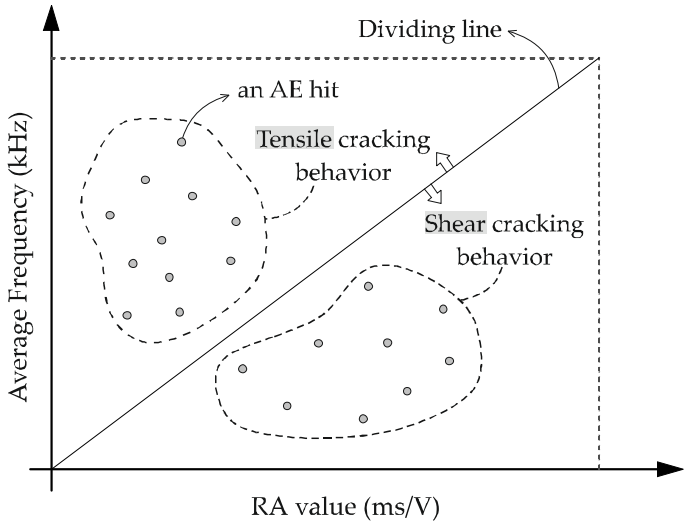

Figure 3. Crack classification by tensile and shear types. (In some references, including [53], other types of cracks are identified instead of shear cracks).

3. Results

3.1. Compression Test: Stress–Time and AE Results

Uniaxial compressive strength tests were conducted on cylindrical specimens at 56 days of age, and the results were plotted as compressive stress–time curves. Figures 4 and 5 present the test results for HPC containing basalt fibers and synthetic macro fibers, respectively. In plot (a) of both figures, the results for plain HPC (without fibers) are provided for comparison. As illustrated, alongside the compressive stress–time curve, the cumulative AE count–time and AE energy–time curves are also plotted, allowing for the observation of AE signal variations in response to the compressive stress changes in the cylindrical specimens. To facilitate better interpretation and comparison of the results, the vertical and horizontal scales of all relevant graphs in these experiments were kept consistent.

The curves in Figure 4 demonstrate that as the basalt fiber content increased from 0% to 2.5%, the compressive strength of HPC decreased from 99.8 MPa to 85.8 MPa, reflecting a reduction of approximately 14%. For samples containing 1.5% fibers, the strength loss was 1.5%. The analysis of AE count and energy curves revealed that higher fiber content led to an increase in cumulative AE counts as the load approached the peak compressive strength; however, the AE energy exhibited a decreasing trend. Beyond the peak strength, the post-failure behavior of these curves varied depending on the crushing mechanism of the concrete. A consistent observation across all AE test results, particularly in the energy–time curves, is that the cumulative AE indices during the first quarter to one-third of the test duration were negligible compared to their final values, followed by a progressive and marked increase thereafter.

The compressive and acoustic emission test results for specimens containing synthetic macro fibers, presented in Figure 5, demonstrate that adding 1.5%, 2%, and 2.5% volumetric fiber content to HPC leads to maximum compressive strength reductions of 4.8%, 6.5%, and 9.6%, respectively. Similarly to the effect of basalt fibers on the stress–strain behavior of this concrete type, the synthetic macro fibers reduced the overall slope of the curve near the peak load, with this effect becoming more pronounced at higher fiber contents. This observation highlights the role of fibers in enhancing the ductility of specimens under compression. Furthermore, the acoustic emission test results indicate that increasing the fiber content resulted in a decrease in cumulative AE counts and energy at peak loads. This is consistent with the findings for HPC-BF compressive specimens; the AE energy released during the elastic phase of HPC-SMF behavior was significantly lower compared to subsequent phases.

This aligns with the definitions of concrete behavior under compression in the elastic region and the principles governing AE wave propagation.

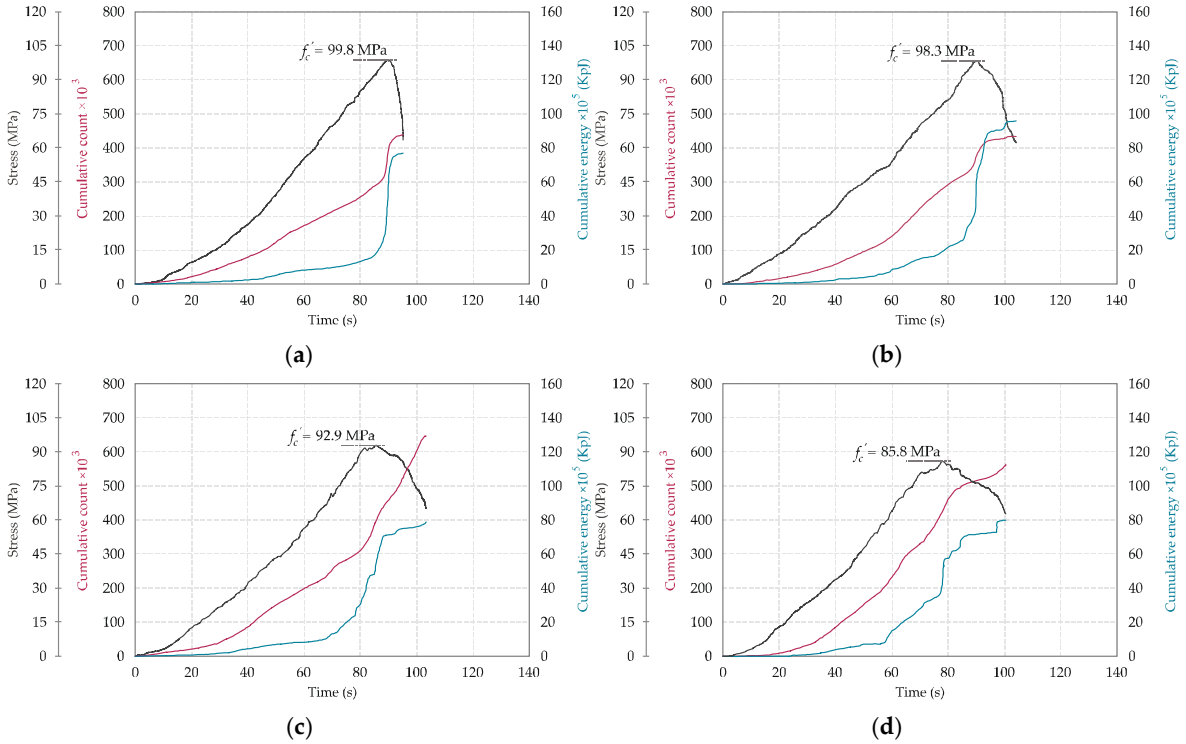

Figure 4. Damage development during uniaxial compression tests monitored by AE analysis: (**a**) HPC without fiber; (**b**) 1.5% BF; (**c**) 2.0% BF; and (**d**) 2.5% BF. Curves: load time (black), cumulative AE count (red), cumulative AE energy (blue).

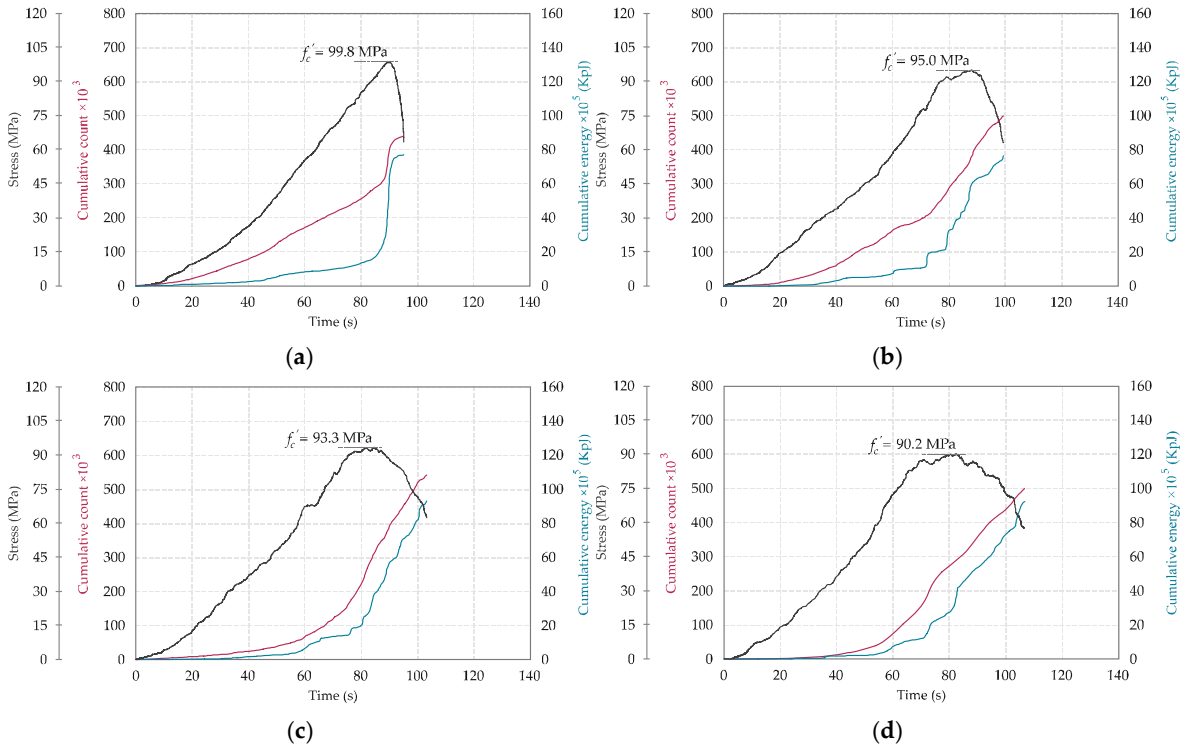

Figure 5. Damage development during uniaxial compression tests monitored by AE analysis: (**a**) HPC without fiber; (**b**) 1.5% SMF; (**c**) 2.0% SMF; and (**d**) 2.5% SMF. Curves: load time (black), cumulative AE count (red), and cumulative AE energy (blue).

3.2. Flexural Toughness Test: Stress–Time and AE Results

Figures 6 and 7 present the flexural toughness test results for HPC-BF and HPC-SMF specimens at 56 days, respectively. The four-point bending stress–time curves are plotted alongside cumulative AE test results, including both count–time and energy–time curves. To facilitate better interpretation and comparison of the results, the vertical axis scale was standardized across all flexural strength test diagrams. However, the horizontal axis scales vary between specimens containing basalt fibers, synthetic macro fibers, and plain concrete due to differences in the time to reach peak load and post-peak load degradation behavior.

The analysis of the graphs in Figure 6 reveals that the addition of 1.5% basalt fibers to the HPC mix leads to an increase in flexural strength of up to 18.6%. This enhancement rises to 58.7% and 72.5% for fiber contents of 2.0% and 2.5%, respectively. Moreover, the inclusion of fibers significantly improves the ductility of the specimens. In the plain (unreinforced) specimen, the sample fractured into two pieces immediately after reaching the peak load. In contrast, with the addition and increased volume of basalt fibers, the specimens sustained higher loads over longer durations, resulting in a greater area under the load–time curve. This trend is also distinctly observed in acoustic emission characteristics, especially the energy curves. In the plain specimen, these curves exhibited sudden jumps at peak load. In contrast, in fiber-reinforced specimens, the energy was released gradually and in a stepwise fashion throughout the test duration.

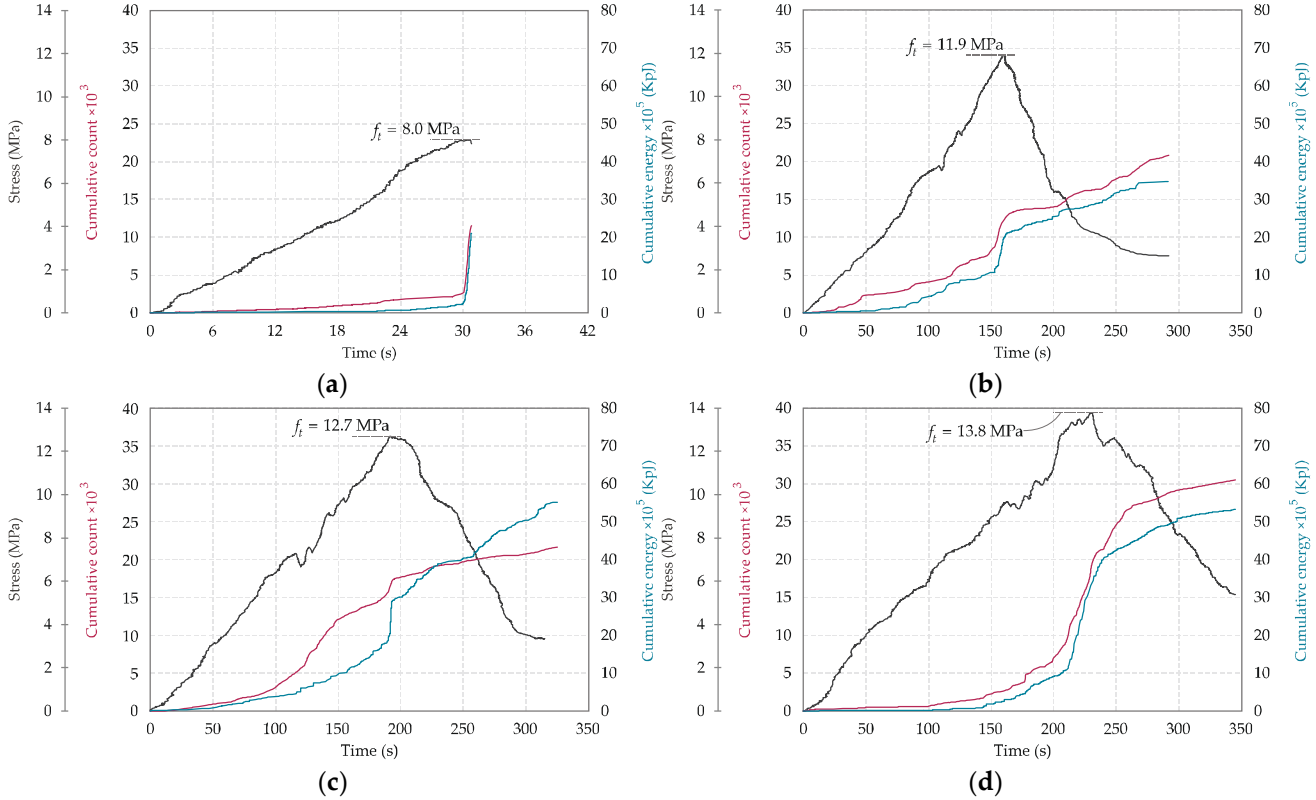

Figure 6. Damage development during 4-point bending tests monitored by AE analysis: (**a**) HPC without fiber; (**b**) 1.5% BF; (**c**) 2.0% BF; and (**d**) 2.5% BF. Curves: load time (black), cumulative AE count (red), and cumulative AE energy (blue).

The flexural test results of HPC-SMF specimens presented in Figure 7 demonstrate a significant enhancement in flexural strength ranging from 8.7% to 46.2% with the incorporation of 1.5% to 2.5% synthetic macro fibers in HPC. While the overall behavior of the count and energy curves in these flexural specimens closely resembled that of HPC-BF specimens, quantitative analysis revealed consistently lower AE count and energy values

for macro fiber-reinforced concretes. The fiber bridging effects during various cracking stages are particularly evident in the characteristic stepwise progression of AE energy curves, which directly correlates with the load drops observed in the stress–time curves. This distinctive stair-step pattern in AE energy release can be primarily attributed to the progressive debonding and pull-out mechanisms of fibers from the cementitious matrix, where each energy plateau corresponds to individual fiber–matrix interfacial failure events, followed by subsequent stress redistribution. Furthermore, the reduced AE activity in SMF specimens compared to BF-reinforced specimens suggests potentially different microfracture mechanisms and energy dissipation patterns, possibly due to variations in fiber–matrix interfacial properties and bond characteristics between the two fiber types. These observations collectively highlight the crucial role of fiber reinforcement in modifying both the macroscopic mechanical properties and microscopic damage evolution processes in high-performance fiber-reinforced concrete systems.

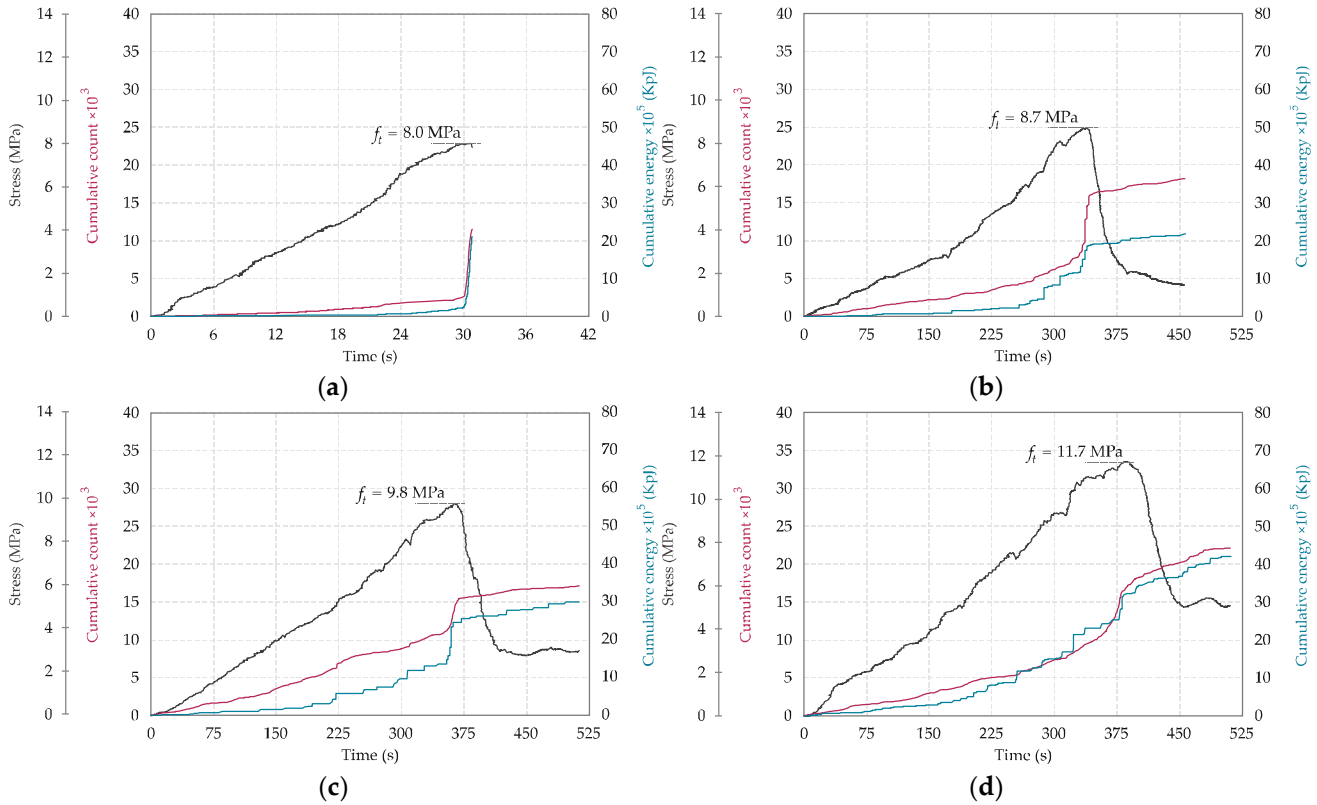

Figure 7. Damage development during 4-point bending tests monitored by AE analysis: (**a**) HPC without fiber; (**b**) 1.5% SMF; (**c**) 2.0% SMF; and (**d**) 2.5% SMF. Curves: load time (black), cumulative AE count (red), and cumulative AE energy (blue).

3.3. Crack-Type Classification

Following the methodology outlined in ISO 16838:2019 [53], AE events were systematically classified during both uniaxial compressive strength tests and four-point bending tests to quantify the proportion of tensile cracks relative to the total number of cracking events up to the peak load. For this purpose, RA and FA values were first calculated for each recorded AE hit during testing, and crack types were identified according to Figure 3. Subsequently, the number of tensile-type hits was divided by the total number of hits. Figure 8 illustrates these findings for the compressive strength tests. The bar chart analysis reveals that although HPC specimens were subjected to compressive loading, the predominant crack type observed was tensile cracking. With the notable exception of specimens containing 2% synthetic macro fibers, the data demonstrate a consistent reduction in tensile

crack occurrence with an increasing fiber content. Comparative analysis indicates that synthetic macro fibers exhibit superior performance to basalt fibers in reducing the ratio of tensile AE events to the total recorded AE activity, suggesting more effective crack-bridging capabilities in macro fiber-reinforced composites. This differential behavior underscores the importance of selecting the appropriate fiber type to optimize the fracture resistance of high-performance concrete systems.

Figure 9 presents the crack classification results from the flexural strength tests. Given that all specimens, including the plain concrete sample, failed in the middle third span under flexural mode, a classification index value exceeding 0.5, as shown in the graph, was expected as the normative baseline. The results demonstrate how incorporating fiber into HPC specimens led to a marked increase in tensile crack formation, with this effect being more pronounced in basalt fiber-reinforced composites compared to other fiber types. The observed elevation in tensile cracking propensity, particularly evident in basalt fiber specimens, suggests that while fibers generally enhance ductility, their specific material properties significantly influence the fracture mechanics and crack propagation patterns under flexural loading conditions.

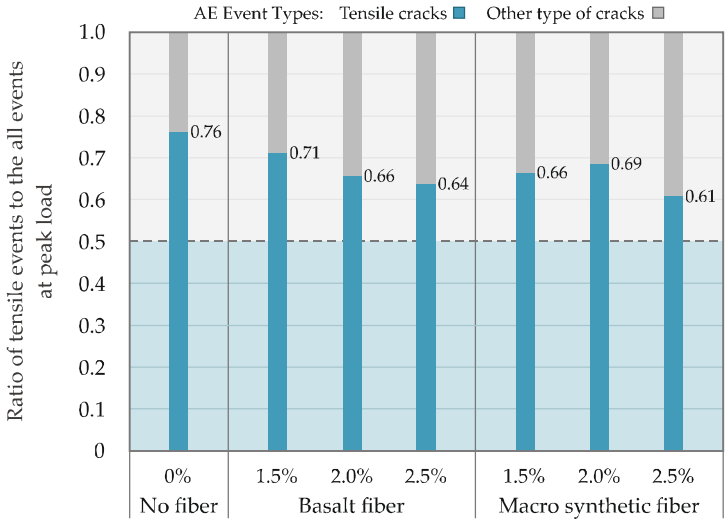

Figure 8. The ratio of tensile events to all emitted events at peak load for each of the compression tests.

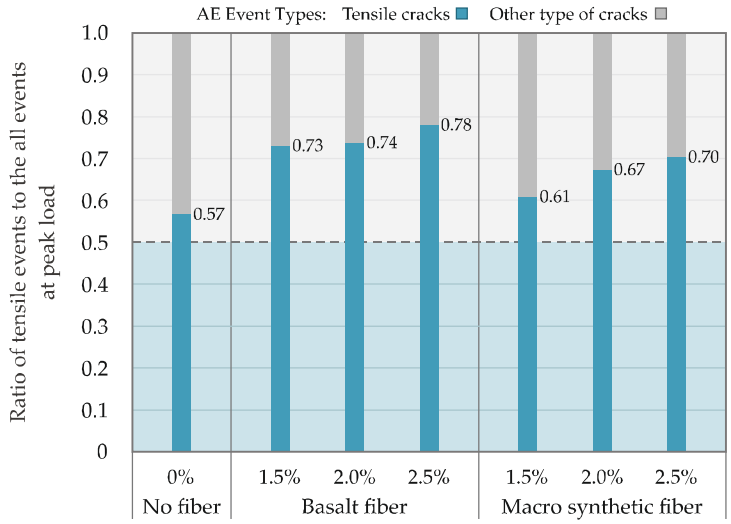

Figure 9. The ratio of tensile events to all emitted events at peak load for each of the flexural tests.

4. Discussion

The cracking behavior observed in HPC under mechanical loading, as assessed via acoustic emission monitoring, offers valuable insights into the failure mechanisms and the role of fiber reinforcement in enhancing structural integrity. The following sub-sections provide a more detailed analysis of the results related to concrete cracking observed in both compressive and flexural toughness tests.

4.1. Compressive Behavior and AE Response

Under compressive loading, although the applied stress is nominally compressive, AE analysis revealed that the majority of emitted signals corresponded to tensile cracking. This phenomenon can be attributed to the lateral tensile stresses induced by the Poisson effect, which promote the initiation and propagation of microcracks perpendicular to the compressive axis. The predominance of tensile-type AE signals, particularly in plain concrete specimens, underscores the vulnerability of unreinforced HPC to brittle failure characterized by sudden energy release and unstable crack growth.

The incorporation of basalt and synthetic macro fibers substantially altered the cracking dynamics. Specifically, the AE data showed that the increased fiber content delayed the onset of rapid energy release and promoted a more gradual accumulation of AE events, indicating distributed microcracking and improved energy dissipation. In compression, the addition of fibers led to a slight reduction in both peak strength and cumulative AE energy. This observation is consistent with previous findings [21], indicating that increasing the fiber content results in higher water absorption and porosity in concrete. Moreover, the density of the specimens in this study decreased with higher fiber content percentages. A comparison between the theoretical and experimental densities of the fabricated specimens, based on fiber density, further confirms the increase in porosity.

On the other hand, fiber inclusion significantly enhanced post-peak ductility, as evidenced by smoother AE energy–time curves and reduced event severity. This suggests that fibers, particularly synthetic macro fibers with better crack-bridging capabilities, contribute to arresting crack propagation and redistributing stresses more effectively within the matrix due to their higher aspect ratio and superior bonding characteristics.

4.2. Flexural Behavior and AE Response

In flexural toughness tests, the fiber-reinforced specimens exhibited dramatic improvements in both load-carrying capacity and ductility. The AE data clearly distinguish the brittle fracture behavior of plain concrete from the more controlled cracking evolution in fiber-modified specimens. Unlike the compression tests, in the flexural test, an increase in the fiber content led to a corresponding rise in both the cumulative AE energy and the cumulative AE count at the peak load. The incremental increases in AE energy observed in the reinforced samples correlate with progressive fiber pull-out and debonding mechanisms, which are essential for sustaining residual strength and delaying catastrophic failure. Interestingly, basalt fibers resulted in higher AE activity compared to synthetic macro fibers, which may be attributed to differences in fiber–matrix interfacial bonding and the stiffer nature of basalt fibers, potentially leading to more pronounced microfracture development. This issue was previously demonstrated by the authors in ref. [21] through scanning electron microscope (SEM) images of this type of concrete, showing that the fiber type affects not only the fiber–matrix interface but also the microstructure of the CaO-activated slag-based concrete matrix itself.

5. Conclusions

This study investigated the fracture behavior of cement-free high-performance concrete made with calcium oxide-activated slag and reinforced with synthetic macro and natural basalt fibers, using the acoustic emission technique. Seven mix designs were prepared with fiber volumes of 1.5%, 2.0%, and 2.5%, and tested under uniaxial compression and four-point bending. AE monitoring during mechanical tests enabled the real-time analysis of cracking behavior through key parameters such as count, energy, duration, and amplitude.

AE data revealed the following:

- At peak load, the total recorded AE count and energy in compression tests were higher than those in the corresponding flexural tests, which is expected due to different failure mechanisms.
- Increasing the fiber content reduced the cumulative AE energy at failure in compressive specimens, indicating the fibers' role in force redistribution and altering the failure pattern.
- In flexure, fiber-reinforced specimens exhibited more gradual and uniform AE energy release, especially for those with synthetic fibers.
- The increase in microcracks during bending prevented sudden AE energy surges, resulting in stepwise energy accumulation curves, which were more evident in synthetic macro fiber-reinforced specimens.
- AE also successfully distinguished elastic and plastic regions in the load–displacement response, demonstrating its sensitivity to damage evolution.

Regarding crack type identification, the following points were found:

- A higher fiber content reduced tensile cracking during compression, with synthetic fibers being more effective, though tensile cracks still dominated at peak loads.
- In flexural tests, 1.5% basalt fibers increased flexural strength by ~49% and tensile crack events by 28%, indicating improved ductility. Synthetic fibers had a smaller effect on strength but extended test durations, suggesting better matrix bonding.

This study demonstrates how the AE method can provide real-time insights into damage intensity and failure modes. Beyond its application as a non-destructive testing (NDT) tool for structural and mechanical system monitoring, AE plays a pivotal role in optimizing mix designs. Its key advantage lies in instantaneous and continuous damage detection, distinguishing it from conventional methods. Unlike techniques such as digital image correlation (DIC), which primarily identify macroscopic cracks, AE can detect microcracks at their earliest formation stages. While system setup and calibration present complexities, which are common to most evaluation methods, AE equipment manufacturers have developed user-friendly software to streamline data interpretation. These multifaceted benefits have established AE as a critical tool not only for monitoring urban infrastructure (e.g., bridges) but also for industrial applications, including tanks, offshore platforms, drilling tools, and pipelines.

This research highlights AE as a valuable tool for assessing damage mechanisms and optimizing mix designs in cement-free concrete systems. The application of AE testing for various fiber-reinforced concrete types, including a comparative analysis of Portland cement-based and cement-free concrete systems, the investigation of size effects, and AE signal-based analytical approaches, is essential for future research. Moreover, the simultaneous use of AE with other non-destructive testing techniques could enhance mutual validation and provide a more comprehensive understanding of failure mechanisms.

Author Contributions: Conceptualization, M.A.R. and D.M.; methodology, M.A.R. and H.B.; software, M.A.R.; validation, M.A.R., H.B., and H.M.; formal analysis, M.A.R.; investigation, M.A.R. and

H.B.; resources, M.A.R. and H.M.; data curation, M.A.R.; writing—original draft preparation, M.A.R.; writing—review and editing, D.M. and H.M.; visualization, M.A.R.; supervision, D.M. All authors have read and agreed to the published version of the manuscript.

Funding: This research received no external funding.

Data Availability Statement: The data presented in this study are available upon request from the corresponding author. The data are not publicly available due to confidentiality issues.

Conflicts of Interest: The authors declare that they have no conflicts of interest.

Abbreviations

The following abbreviations are used in this manuscript:

AE	Acoustic emission
AF	Average frequency
BF	Basalt fiber
DAQ	Data acquisition (system)
DIC	Digital image correlation
HDT	Hit definition time
HLT	Hit lockout time
HPC	High-performance concrete
ITZ	Interfacial transition zone
NDT	Non-destructive testing
PDT	Peak definition time
PLB	Pencil-lead break
RA	Rise angle
SEM	Scanning electron microscope
SMF	Synthetic macro fiber
UHPC	Ultra-high-performance concrete

References

1. Zhang, J.; Peng, L.; Wen, S.; Huang, S. A Review on Concrete Structural Properties and Damage Evolution Monitoring Techniques. *Sensors* **2024**, *24*, 620. [CrossRef] [PubMed]
2. Lu, C.-G.; Zhang, X.-C.; Chen, W.-Z.; Chen, X.-F. Quantitative Analysis of Crack Propagation Behavior in Recycled Concrete Subjected to Axial Compression Using Digital Image Correlation (DIC) Technology and Fractal Theory. *Fractal Fract.* **2024**, *8*, 686. [CrossRef]
3. Ji, H.; Yang, X.; Luo, Z.; Bai, F. Tensile fracture property of concrete affected by interfacial transition zone. *Int. J. Concr. Struct. Mater.* **2023**, *17*, 2. [CrossRef]
4. Chen, Q.; Zhang, J.; Wang, Z.; Zhao, T.; Wang, Z. A review of the interfacial transition zones in concrete: Identification, physical characteristics, and mechanical properties. *Eng. Fract. Mech.* **2024**, *300*, 109979. [CrossRef]
5. Jiang, Z.; Huang, Q.; Xi, Y.; Gu, X.; Zhang, W. Experimental study of diffusivity of the interfacial transition zone between cement paste and aggregate. *J. Mater. Civ. Eng.* **2016**, *28*, 04016109. [CrossRef]
6. Marvila, M.T.; de Azevedo, A.R.G.; de Matos, P.R.; Monteiro, S.N.; Vieira, C.M.F. Materials for Production of High and Ultra-High Performance Concrete: Review and Perspective of Possible Novel Materials. *Materials* **2021**, *14*, 4304. [CrossRef] [PubMed]
7. Sohail, M.G.; Wang, B.; Jain, A.; Kahraman, R.; Ozerkan, N.G.; Gencturk, B.; Dawood, M.; Belarbi, A. Advancements in concrete mix designs: High-performance and ultrahigh-performance concretes from 1970 to 2016. *J. Mater. Civ. Eng.* **2018**, *30*, 04017310. [CrossRef]
8. Yan, Z.; Zeng, J.-J.; Zhuge, Y.; Liao, J.; Zhou, J.-K.; Ma, G. Compressive behavior of FRP-confined 3D printed ultra-high performance concrete cylinders. *J. Build. Eng.* **2024**, *83*, 108304. [CrossRef]
9. Zeng, J.-J.; Zeng, W.-B.; Ye, Y.-Y.; Liao, J.; Zhuge, Y.; Fan, T.-H. Flexural behavior of FRP grid reinforced ultra-high-performance concrete composite plates with different types of fibers. *Eng. Struct.* **2022**, *272*, 115020. [CrossRef]
10. Kravchuk, R.; Landis, E.N. Acoustic emission-based classification of energy dissipation mechanisms during fracture of fiber-reinforced ultra-high-performance concrete. *Constr. Build. Mater.* **2018**, *176*, 531–538. [CrossRef]
11. Chen, Y.; Jiao, Y.; Yang, H.; Chen, R. Fracture characteristics and damage evolution of manufactured sand-based ultra-high performance concrete using tensile testing and acoustic emission monitoring. *Constr. Build. Mater.* **2024**, *430*, 136477. [CrossRef]

12. Mostafaei, H.; Kelishadi, M.; Bahmani, H.; Wu, C.; Ghiassi, B. Development of sustainable HPC using rubber powder and waste wire: Carbon footprint analysis, mechanical and microstructural properties. *Eur. J. Environ. Civ. Eng.* **2025**, *29*, 399–420. [CrossRef]
13. Mostafaei, H.; Bahmani, H. Sustainable high-performance concrete using zeolite powder: Mechanical and carbon footprint analyses. *Buildings* **2024**, *14*, 3660. [CrossRef]
14. Mostafaei, H.; Badarloo, B.; Chamasemani, N.F.; Rostampour, M.A.; Lehner, P. Investigating the Effects of Concrete Mix Design on the Environmental Impacts of Reinforced Concrete Structures. *Buildings* **2023**, *13*, 1313. [CrossRef]
15. Mostafaei, H.; Rostampour, M.A.; Chamasemani, N.F.; Wu, C. An In-Depth Exploration of Carbon Footprint Analysis in the Construction Sector with Emphasis on the Dam Industry. In *Carbon Footprint Assessments: Case Studies & Best Practices*; Springer: Berlin/Heidelberg, Germany, 2024; pp. 45–80.
16. Bahmani, H.; Mostafaei, H. Impact of Fibers on the Mechanical and Environmental Properties of High-Performance Concrete Incorporating Zeolite. *J. Compos. Sci.* **2025**, *9*, 222. [CrossRef]
17. Ambily, P.S.; Ravisankar, K.; Umarani, C.; Dattatreya, J.K.; Iyer, N.R. Development of ultra-high-performance geopolymer concrete. *Mag. Concr. Res.* **2014**, *66*, 82–89. [CrossRef]
18. Wetzel, A.; Middendorf, B. Influence of silica fume on properties of fresh and hardened ultra-high performance concrete based on alkali-activated slag. *Cem. Concr. Compos.* **2019**, *100*, 53–59. [CrossRef]
19. Danish, A.; Ozbakkaloglu, T.; Mosaberpanah, M.A.; Salim, M.U.; Bayram, M.; Yeon, J.H.; Jafar, K. Sustainability benefits and commercialization challenges and strategies of geopolymer concrete: A review. *J. Build. Eng.* **2022**, *58*, 105005. [CrossRef]
20. Shi, C.; Qu, B.; Provis, J.L. Recent progress in low-carbon binders. *Cem. Concr. Res.* **2019**, *122*, 227–250. [CrossRef]
21. Bahmani, H.; Mostofinejad, D. Novel UHPC with calcium-oxide-activated materials and fibres: Engineering properties and sustainability evaluation. *Mag. Concr. Res.* **2024**, *76*, 882–902. [CrossRef]
22. Rostampour, M.A.; Mostofinejad, D. Acoustic Emission-Based Structural Evaluation of RC Beams with and without FRP Strengthening Under Monotonic Loading. In Proceedings of the Second International Conference on the Exchange of Scientific Information in the Fields of Concrete Structures and Materials (ICConcrete), Tehran, Iran, 7 May 2025.
23. De Rosa, I.M.; Santulli, C.; Sarasini, F. Acoustic emission for monitoring the mechanical behaviour of natural fibre composites: A literature review. *Compos. Part A Appl. Sci. Manuf.* **2009**, *40*, 1456–1469. [CrossRef]
24. Philippidis, T.; Aggelis, D. Experimental study of wave dispersion and attenuation in concrete. *Ultrasonics* **2005**, *43*, 584–595. [CrossRef] [PubMed]
25. Li, D.; Yang, K.; He, Z.; Zhou, H.; Li, J. Acoustic Emission Wave Velocity Attenuation of Concrete and Its Application in Crack Localization. *Sustainability* **2020**, *12*, 7405. [CrossRef]
26. Di Benedetti, M.; Loreto, G.; Matta, F.; Nanni, A. Acoustic emission monitoring of reinforced concrete under accelerated corrosion. *J. Mater. Civ. Eng.* **2013**, *25*, 1022–1029. [CrossRef]
27. Kawasaki, Y.; Wakuda, T.; Kobarai, T.; Ohtsu, M. Corrosion mechanisms in reinforced concrete by acoustic emission. *Constr. Build. Mater.* **2013**, *48*, 1240–1247. [CrossRef]
28. Suzuki, T.; Ogata, H.; Takada, R.; Aoki, M.; Ohtsu, M. Use of acoustic emission and X-ray computed tomography for damage evaluation of freeze-thawed concrete. *Constr. Build. Mater.* **2010**, *24*, 2347–2352. [CrossRef]
29. Zaki, A.; Chai, H.K.; Aggelis, D.G.; Alver, N. Non-Destructive Evaluation for Corrosion Monitoring in Concrete: A Review and Capability of Acoustic Emission Technique. *Sensors* **2015**, *15*, 19069–19101. [CrossRef] [PubMed]
30. Moradian, Z.; Li, B.Q. Hit-based acoustic emission monitoring of rock fractures: Challenges and solutions. In *Advances in Acoustic Emission Technology: Proceedings of the World Conference on Acoustic Emission–2015*; Springer: Berlin/Heidelberg, Germany, 2017; pp. 357–370.
31. Dzaye, E.D.; De Schutter, G.; Aggelis, D.G. Monitoring early-age acoustic emission of cement paste and fly ash paste. *Cem. Concr. Res.* **2020**, *129*, 105964. [CrossRef]
32. Rostampour, M.A.; Mostofinejad, D.; Arefian, B. Effect of Thermal Load on the Parametric Analysis of Acoustic Emission Signals in Concrete. In Proceedings of the Second International Conference on the Exchange of Scientific Information in the Fields of Concrete Structures and Materials (ICConcrete), Tehran, Iran, 7 May 2025.
33. *ASTM C494/C494M-24*; Standard Specification for Chemical Admixtures for Concrete. ASTM: West Conshohocken, PA, USA, 2024.
34. Guerini, V.; Conforti, A.; Plizzari, G.; Kawashima, S. Influence of steel and macro-synthetic fibers on concrete properties. *Fibers* **2018**, *6*, 47. [CrossRef]
35. Nana, W.; Tran, H.; Goubin, T.; Kubisztal, G.; Bennani, A.; Bui, T.; Cardia, G.; Limam, A. Behaviour of macro-synthetic fibers reinforced concrete: Experimental, numerical and design code investigations. *Structures* **2021**, *32*, 1271–1286. [CrossRef]
36. Kazmi, S.M.S.; Munir, M.J.; Wu, Y.-F.; Patnaikuni, I. Effect of macro-synthetic fibers on the fracture energy and mechanical behavior of recycled aggregate concrete. *Constr. Build. Mater.* **2018**, *189*, 857–868. [CrossRef]
37. Zheng, Y.; Zhang, Y.; Zhuo, J.; Zhang, Y.; Wan, C. A review of the mechanical properties and durability of basalt fiber-reinforced concrete. *Constr. Build. Mater.* **2022**, *359*, 129360. [CrossRef]

38. Vatin, N.I.; Hematibahar, M.; Gebre, T.H. Impact of basalt fiber reinforced concrete in protected buildings: A review. *Front. Built Environ.* **2024**, *10*, 1407327. [CrossRef]
39. *ASTM C1437-20*; Standard Test Method for Flow of Hydraulic Cement Mortar. ASTM: West Conshohocken, PA, USA, 2020.
40. *ASTM C39/C39M-24*; Standard Test Method for Compressive Strength of Cylindrical Concrete Specimens. ASTM: West Conshohocken, PA, USA, 2024.
41. *ASTM C78/C78M-22*; Standard Test Method for Flexural Strength of Concrete (Using Simple Beam with Third-Point Loading). ASTM: West Conshohocken, PA, USA, 2022.
42. *ASTM E750-15(2020)*; Standard Practice for Characterizing Acoustic Emission Instrumentation. ASTM: West Conshohocken, PA, USA, 2020.
43. Physical Acoustics Corporation. *PCI-2 Based AE System User's Manual*; Physical Acoustics Corporation: West Windsor Township, NJ, USA, 2007.
44. *ISO 16836:2019*; Non-Destructive Testing—Acoustic Emission Testing—Measurement Method for Acoustic Emission Signals in Concrete. ISO: Geneva, Switzerland, 2019.
45. *ASTM E976-15(2021)*; Standard Guide for Determining the Reproducibility of Acoustic Emission Sensor Response. ASTM: West Conshohocken, PA, USA, 2021.
46. Ohno, K.; Ohtsu, M. Crack classification in concrete based on acoustic emission. *Constr. Build. Mater.* **2010**, *24*, 2339–2346. [CrossRef]
47. Behnia, A.; Chai, H.K.; Shiotani, T. Advanced structural health monitoring of concrete structures with the aid of acoustic emission. *Constr. Build. Mater.* **2014**, *65*, 282–302. [CrossRef]
48. Carpinteri, A.; Lacidogna, G.; Accornero, F.; Mpalaskas, A.; Matikas, T.; Aggelis, D. Influence of damage in the acoustic emission parameters. *Cem. Concr. Compos.* **2013**, *44*, 9–16. [CrossRef]
49. Rather, A.I.; Mirgal, P.; Banerjee, S.; Laskar, A. Application of acoustic emission as damage assessment technique for performance evaluation of concrete structures: A review. *Pract. Period. Struct. Des. Constr.* **2023**, *28*, 03123003. [CrossRef]
50. Aggelis, D.G.; Shiotani, T. Parameters based AE analysis. In *Acoustic Emission Testing: Basics for Research–Applications in Engineering*; Springer: Berlin/Heidelberg, Germany, 2021; pp. 45–71.
51. Sagar, R.V.; Prasad, B.R. A review of recent developments in parametric based acoustic emission techniques applied to concrete structures. *Nondestruct. Test. Eval.* **2012**, *27*, 47–68. [CrossRef]
52. *JCMS-III B5706*; Monitoring Method for Active Cracks in Concrete by Acoustic Emission. Federation of Construction Materials Industries: Tokyo, Japan, 2003.
53. *ISO 16838:2019*; Non-Destructive Testing—Acoustic Emission Testing—Test Method for Classification of Active Cracks in Concrete Structures. ISO: Geneva, Switzerland, 2019.

Disclaimer/Publisher's Note: The statements, opinions and data contained in all publications are solely those of the individual author(s) and contributor(s) and not of MDPI and/or the editor(s). MDPI and/or the editor(s) disclaim responsibility for any injury to people or property resulting from any ideas, methods, instructions or products referred to in the content.